Numerical Analysis on the Use of Carbon Nanostructures as Interlayers to Perovskite Solar Cells Using SCAPS-1D

Wisly Fidel, Guido Perrin, Ikram Anefnaf, Richard K Koech, Dieuseul Prédélus, Nicole Doumit, Jacques Botsoa, Conchi Maria Concepcion Ovin Ania, Esidor Ntsoenzok

ADVANCED THEORY AND SIMULATIONS
www.advtheorysimul.com

Numerical Analysis on the Use of Carbon Nanostructures as Interlayers to Perovskite Solar Cells Using SCAPS-1D

Wisly Fidel, Guido Perrin, Ikram Anefnaf, Richard K Koech, Dieuseul Prédélus, Nicole Doumit, Jacques Botsoa, Conchi O. Ania, and Esidor Ntsoenzok*

Despite the numerous efforts to optimize the performance of perovskite solar cells (PSCs), challenges persist. Carbon materials are promising candidates for this purpose, but identifying the most suitable carbon material and understanding its role in the PSC among the wide family of carbons remains a challenging task. In this study, SCAPS-1D software is employed to optimize the use of carbon materials as interlayers to PSCs. The best configuration of the carbon interlayer and the required physicochemical properties of the carbon materials is identified for improved performance. The simulations show that the insertion of thin carbon interlayers of adequate features in n-i-p stacked cells (FTO/TiO_2/$MAPbI_3$/HTL/Ni) can increase the efficiency of the resulting PSCs by over 2.3 %, while significantly improving the open-circuit voltage and the fill factor. These results underline that those carbon materials with optical bandgaps ranging from 3 to 3.5 eV offer the best performance as an interlayer to the hole tranport layer, with negligible impact of the thickness of the interlayer. This contribution offers a novel perspective on the use of carbon materials in PSCs and provides new insights into the understanding of the role of carbon materials as interlayers in PSCs.

1. Introduction

About 85% of current global energy outputs from the combustion of fossil fuels, which are not only exhaustible resources but contribute to the growing impact of global warming.[1] Furthermore, the world population expansion in the next 50 years is expected to be more than 23%, which will also accelerate the global energy demand.[2,3] To ensure a sustainable production of electricity complying with economic growth, consumption needs, and environmental concerns, the use of renewable sources and, in particular, the conversion of solar energy is considered one of the best alternatives. The earth receives $\approx 1.8 \times 10^{14}$ kWs^{-1} of solar energy per year, and it is estimated that the amount per hour is sufficient to meet the needs of humanity for more than a year.[4] Since the pioneering work of Kojima et al., perovskite solar cells (PSCs) have attracted significant attention as a viable solar energy harvesting technology.[5,6] They offer an attractive combination of cost-effectiveness and superior conversion efficiency, positioning them at the forefront of sustainable energy solutions. PSCs are composed of an absorber (the perovskite) layer encapsulated between two oppositely doped charge selective layers to form (regular) n-i-p or (inverted) p-i-n device architectures, with two appropriate electrodes where electrons and holes are collected as electric current.[7] The efficiency of PSCs has continued to increase and currently stands at a laboratory scale of 26.1% for a n-i-p, 25.52% for a p-i-n single junction, and 33.9% for a perovskite/silicon tandem.[8,9] This accelerated progress has been attributed to the perovskite's excellent properties such as high optical absorption, long carrier diffusion length, high defect tolerance that reduces recombination losses, small exciton dissociation energy, and flexibility of composition by solution-based synthesis, among others.[10,11]

W. Fidel, G. Perrin, J. Botsoa, C. O. Ania, E. Ntsoenzok
CEMHTI (UPR 3079, CNRS)
Université d'Orléans
1 AV. de la Recherche Scientifique, Orléans 45100, France
E-mail: wisly.fidel@cnrs-orleans.fr

The ORCID identification number(s) for the author(s) of this article can be found under https://doi.org/10.1002/adts.202400771

DOI: 10.1002/adts.202400771

W. Fidel, D. Prédélus
Dept. Physique, Université d'Etat d'Haïti-Ecole Normale Supérieure
Laboratoire des Sciences pour l'Environnement et l'Energie (LS2E)
Canapé-Vert, Port-au-Prince HT6115, Haïti

I. Anefnaf
LAPS-Laboratory for Photovoltaics and solid-state Physics
Dept. Computer Science
University of Verona
Strada le Grazie 15, Verona 37134, Italy

R. K Koech
Dept. Mathematics, Physics and Computing
Moi University
Eldoret 3900–30100, Kenya

N. Doumit
LISITE Laboratory
ISEP
10 Rue de Vanves, Issy-les-Moulineaux 92130, France

Electron transport layers (ETLs) and hole transport layers (HTLs) are also among the various factors affecting the performance of PSCs. These layers are typically doped to achieve an optimal performance but suffer from severe degradation.[12] To overcome this limitation, significant research efforts are being focused on modifying the composition of these layers through doping or incorporating interlayers. Among different options, the use of carbon nanostructures as interlayers and additives to the HTL and ETL has attracted attention in the past decades, owing to their high chemical stability, abundance, and favorable optoelectronic features.[13,14] As a few examples, Widianto et al., reported the use of graphene oxide as HTL for carbon-based mesoscopic PSCs; the authors also highlighted the beneficial effect of graphene oxide on the quality of the perovskite film, resulting in larger grain sizes and fewer pinholes.[14] Mariani et al., reported the improved efficiency of low-temperature graphene-based pastes for fabricating stable carbon-based PSCs.[15] The incorporation of carbon nanotubes into polymer HTL has been shown to enhance the stability of the layers due to the compact nature and strong interaction with the carbon nanotubes and to reduce the cost of the solar cell by more than 5.5%.[16] Tian et al., have reported optimal hole extraction in perovskite/oxidized carbon black interfaces, resulting in an improved efficiency of more than 2% compared to the control device.[17] The potential of graphene, carbon nanotubes, and carbon quantum dots as interlayers at perovskite interfaces and as HTL has also been reported in the literature, with emphasis on the importance of the concentration of traps to achieve a good carrier collection and passivation of grain boundaries of the perovskite layer.[18,19,13,20–23]

Despite the promising results reported for various carbon nanostructures, there is a lack of understanding of the underlying mechanism of these materials as interlayers. This is mostly due large variability of carbon materials, and the lack of systematic studies taking into account their electronic and optical properties. Indeed, a wide variety of carbon materials and allotropic forms with very different properties exist depending on the spatial arrangement of carbon atoms and the presence of heteroatoms. As a result, carbon nanostructures can display very different structures, electronic conductivity, optoelectronic properties, and reactivity (among others). As examples, some carbons present a high electron mobility similar to that of metals (e.g., graphene, carbon blacks, carbon nanotubes), while other carbons are moderate or poorly conductive (e.g., porous carbons, chars) or insulators (e.g., diamond, hydrochars, graphene oxides and reduced graphene oxides). All these features are essential for the performance of solar cells. Another important issue is the position of the carbon interlayer in the PSC; different simulation and experimental works have reported promising results in either position, without a proper rationalization of such behavior. It is evident that the performance of a carbon interlayer in PSCs (or other solar cells) will strongly depend on the physicochemical characteristics of the carbon material, but identifying the best carbon interlayer among the wide family of carbons is a challenging, often neglected task.

Considering all the above, in this work we have used numerical simulations with SCAPS-1D software to rationalize the role of carbon nanostructures with diverse electronic and optical properties as interlayers of HTL in PSCs. Our simulations show that incorporating a thin carbon interlayer with an optical bandgap ranging from 3 to 3.5 eV to spiro-OMeTAD as HTL in a regular n-i-p stacked structure ($FTO/TiO_2/MAPbI_3$/HTL-C interlayer/Ni) significantly improves the open-circuit voltage and the fill factor (FF) of the resulting devices, leading to an enhancement of 2.3% in the conversion efficiency. The position of the carbon interlayer is important to ensure a correct balance band offset of the perovskite/hybrid HTL interface and a good extraction of the holes. The best bandgap alignment of the carbon nanostructure and the HTL was obtained for bandgap values ranging from 2.7 to 3.5 eV, which would point out to amorphous carbons, porous carbons, and carbon nanotubes as best candidate nanostructures. Our numerical simulations provide new insights into the use of carbon materials as interlayers in PSCs to reach improved performance.

2. Results and Discussion

The purpose of this study was to evaluate using SCAPS-1D the use of carbon materials as interlayers to the HTL in a perovskite solar cell with a n-i-p stacked structure (FTO/ETL/AL/HTL/BCM). Before this, we have optimized several aspects of the solar cell such as the thickness of the absorber layer and the back contact. The next sections summarize this optimization.

2.1. Optimization of the Absorber Layer Thickness

We initially optimized the thickness of the active layer in an FTO/ETL/AL/HTL/BCM solar cell device. This is important to maximize the current density and to maintain a balance between light absorption and charge carrier generation. **Figure 1** shows the simulated performance of the solar device varying the thickness of the perovskite active layer between 300 and 1200 nm. Increasing the thickness of the active layer (AL) did not modify significantly the open-circuit voltage of the cell but increased the current density with values going from 20.41 to 25.86 mA cm^{-2} for thicknesses of 300 and 1200 nm respectively. The increase was more pronounced for thicknesses between 300 and 700 nm. This behavior aligns with our expectations, indicating that the light absorption capacity of the AL in the studied range of thickness values is increased, without much loss of charge recombination.

The fill factor (FF) decreased by ca. 3%, which indicates a slight increase in the series resistance owing to a less efficient charge carrier extraction at the ETL/perovskite and/or perovskite/HTL interfaces. The conversion efficiency of the cell followed a similar trend to that described for the current density, with an overall increasing trend with the thickness that is more pronounced between 300 and 600 nm, reaching a constant plateau for values above 700 nm. A similar trend has been reported in the literature, for $FTO/ETL/MAPbI_3/NiO_x$/Au configurations, using various ETLs and HTLs.[24]

2.2. Optimization of the Back Contact Metal

The nature of the back contact metal (BCM) used in solar cells has an important role as it may affect the charge accumulation in the cathode (thus the fill factor and the open-circuit

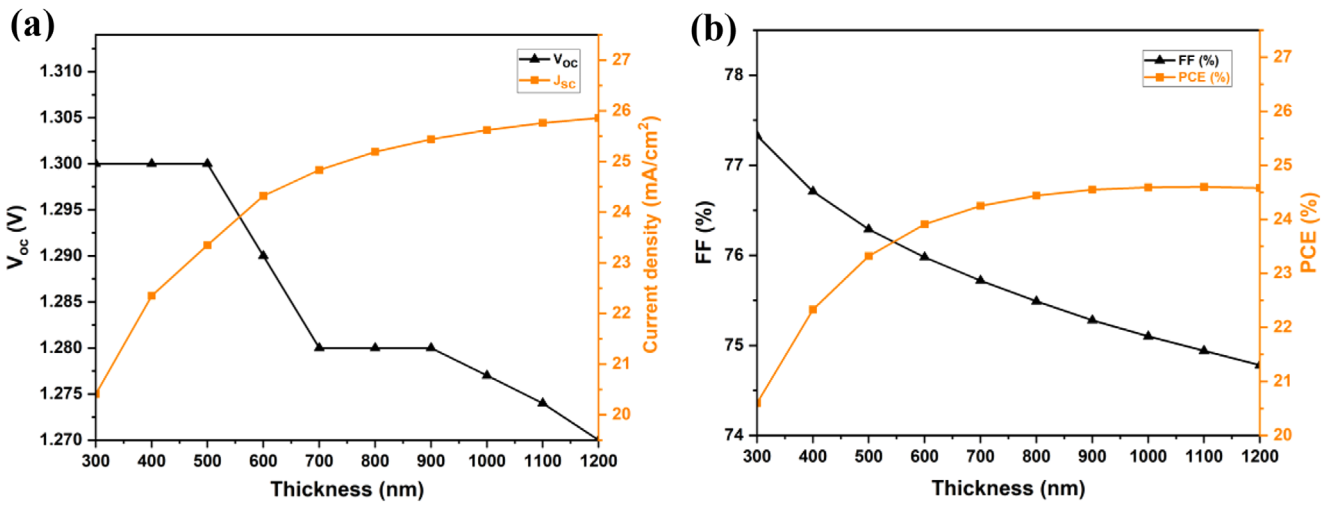

Figure 1. Effect of the absorber layer thickness on the main performance parameters of an FTO/ETL/AL/HTL/BCM solar cell: a) *J–V* curve and open-circuit potential; b) Fill factor (FF) and Power Conversion Efficiency (PCE). The thickness of the ETL and HTL was set to 50 nm, 100 nm, and the BCM was gold.

voltage).[25] In our study, we have simulated the performance of the FTO/ETL/AL/HTL/BCM configuration using noble (Au, Pt) and non-noble metals (Ni, Cu, Cr) as back contact. Obtained data concerning key performance indicators of the device are summarized in **Table 1**. The best cell performance parameters were obtained for Au, Pt, and Ni, the metals with higher work functions. In the case of copper and chromium, their low work function values suggest a lower ability to extract the photogenerated holes, thus the open circuit voltage and conversion efficiency of the solar cell is lower.

Comparatively, the cells built with Pt, Au, and Ni showed similar performance indicators in terms of open-circuit voltage, fill factor, and conversion efficiency. This suggests that metals with work functions between 5.7 and 5.1 eV seem to be adequate for this type of solar cell. We also observed a current density, which is not affected by the choice of the BCM. Given the high cost and scarcity of Pt and Au, we have selected nickel as the back contact metal for this study. Furthermore, it has been reported that Au has some other disadvantages related to an accelerated degradation of perovskite solar cells.[27] The trend observed for BCM like Pt and Ni further supports the results obtained by Deepthi et *al*, whose investigation shows for PSC with an active layer of $MAPbI_3$ and all inorganic charge transport layers (CTLs), the PCE remained constant for all BCM with work function higher than 5.1 eV.[28]

Table 1. Performance parameters of an FTO/ETL/AL/HTL/BCM solar cell varying the nature of the metal used as back contact metal.

Back contact metal	Work function [eV][26]	V_{OC}[V]	J_{SC}[mA/cm^2]	*FF* [%]	PCE[%]
Pt	5.6	1.35	24.83	82.26	27.64
Au	5.10	1.35	24.83	82.26	27.64
Ni	5.15	1.35	24.83	82.26	27.64
Cu	4.65	1.03	24.83	77.44	24.98
Cr	4.50	1.28	24.83	67.27	21.45

2.3. Total Defect Density (Dit) at Different Interfaces

The impact of the total defect density (D_{it}) at the ETL/perovskite and perovskite/HTL interfaces on the performance of the cell is shown in **Figure 2**. The total defect density is an indicator of the energy band alignment between the perovskite and the charge-transport layers that affect the non-radiative recombination losses of the device.[29] The D_{it} of the interlayers varied from 10^9 to $10^{16}cm^{-2}$, while keeping other parameters constant; these values correspond to those widely measured and reported in the literature for these systems.[30–34] As seen in Figure 2a,b, V_{oc} and FF are very sensitive to D_{it} while the current density is mostly not affected (except for very high defects density). V_{oc} decreases significantly with the D_{it} values (going from 1.35 to 1.14 V) which suggests the formation of an energy barrier at the ETL/AL interface when the density of defects is high. This barrier would induce the accumulation of the charge (reverse saturation current), thus reducing V_{oc}.[29]

The FF displayed a wavy dependence with D_{it}, with maximum values for D_{it} in the range 10^{13} –$10^{15}cm^{-2}$, although the variation is subtle (ca. 4%). According to the literature, increasing the defects at the interfaces typically results in an increase in the contact resistance between the perovskite layer and the charge-collecting layers, leading generally to lower FF.[33] Thus, the wavy dependence of the FF with D_{it} may be attributed to an increase in the series resistance of the device or the creation of recombination centers for charge carriers (both can lower the FF). Our simulations are in line with other studies reported in the literature using spiro-OMeTAD as HTL and other inorganic and organic interlayers. As a few examples, Wang et al., reported a ca. 3% increase in the FF using chromium trioxide as HTL interlayer.[35] Zhang et al., reported similar fill factors (83%) but lower open circuit voltage (ca. 1.18 V) when using polar organic molecules as HTL interlayer.[29] The improved Voc in our study is likely due to the reduced contact resistance at the C-layer/Ni interface and/or a decrease in the recombination rate.

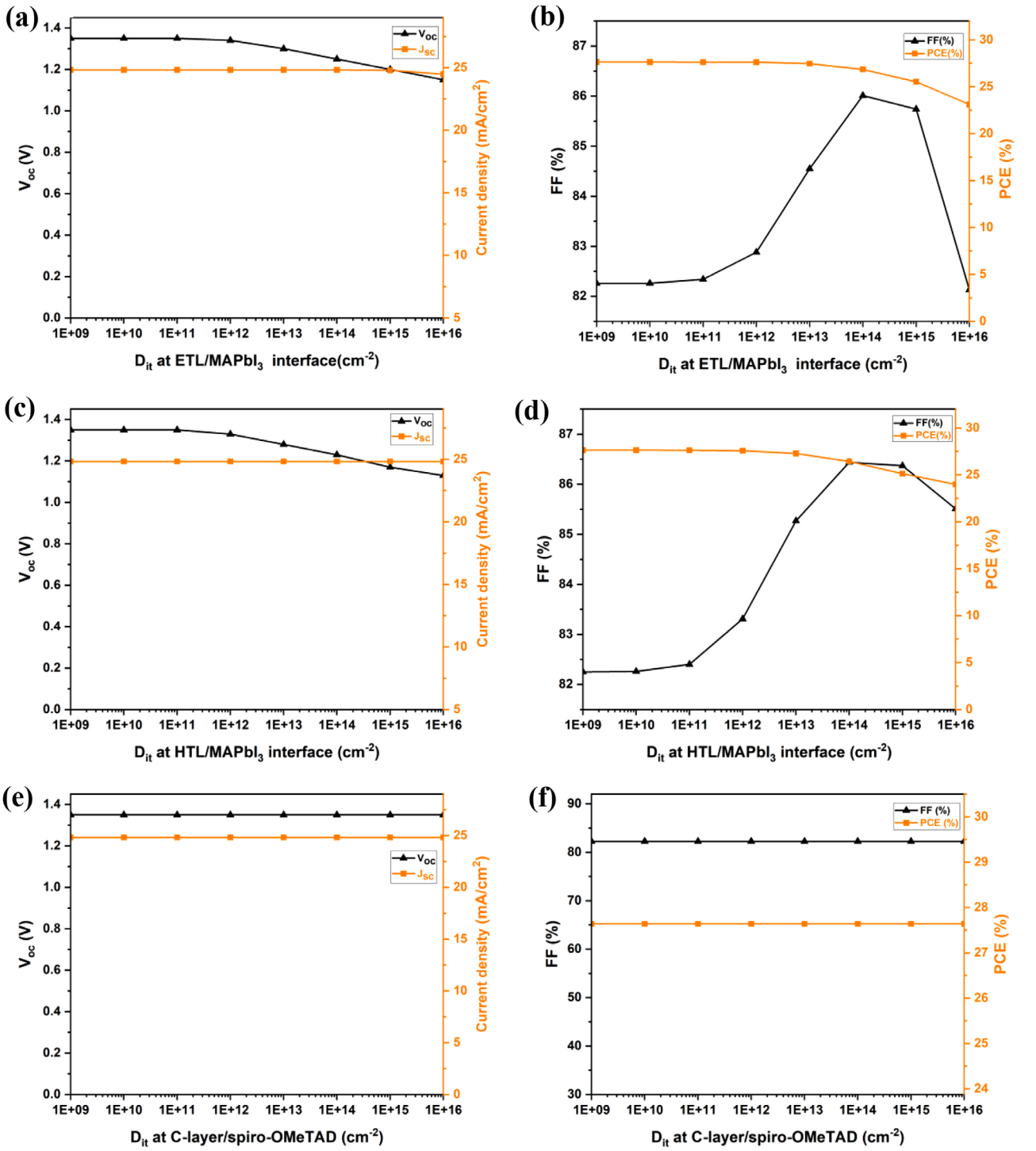

Figure 2. Influence of total defect density (D_{it}) on the performance parameters V_{oc}, J_{sc}, FF and PCE of a PSC: a,b) D_{it} at ETL/perovskite interface; c,d) D_{it} at perovskite/HTL interface; e,f) D_{it} at HTL/C-interlayer interface (fixing the D_{it} at ETL/perovskite and the perovskite/HTL at 10^{-10}cm^{-2} and the thickness of the carbon interlayer at 70 nm).

For the perovskite/HTL, interface (Figure 2c,d), similar trends have been observed with the total density of defects. For the C-interlayer/HTL interface (Figure 2e,f), the density of defects did not seem to affect any of the performance parameters of the solar cell. This points out a good contact between the carbon interlayer and the HTL or the BCM, ensuring efficient charge transfer across the interface. Based on the obtained results, the total defect density at both the ETL/perovskite and perovskite/HTL interfaces was fixed to 10^{10}cm^{-2}, while the C-interlayer/HTL interface was considered as an ohmic contact.

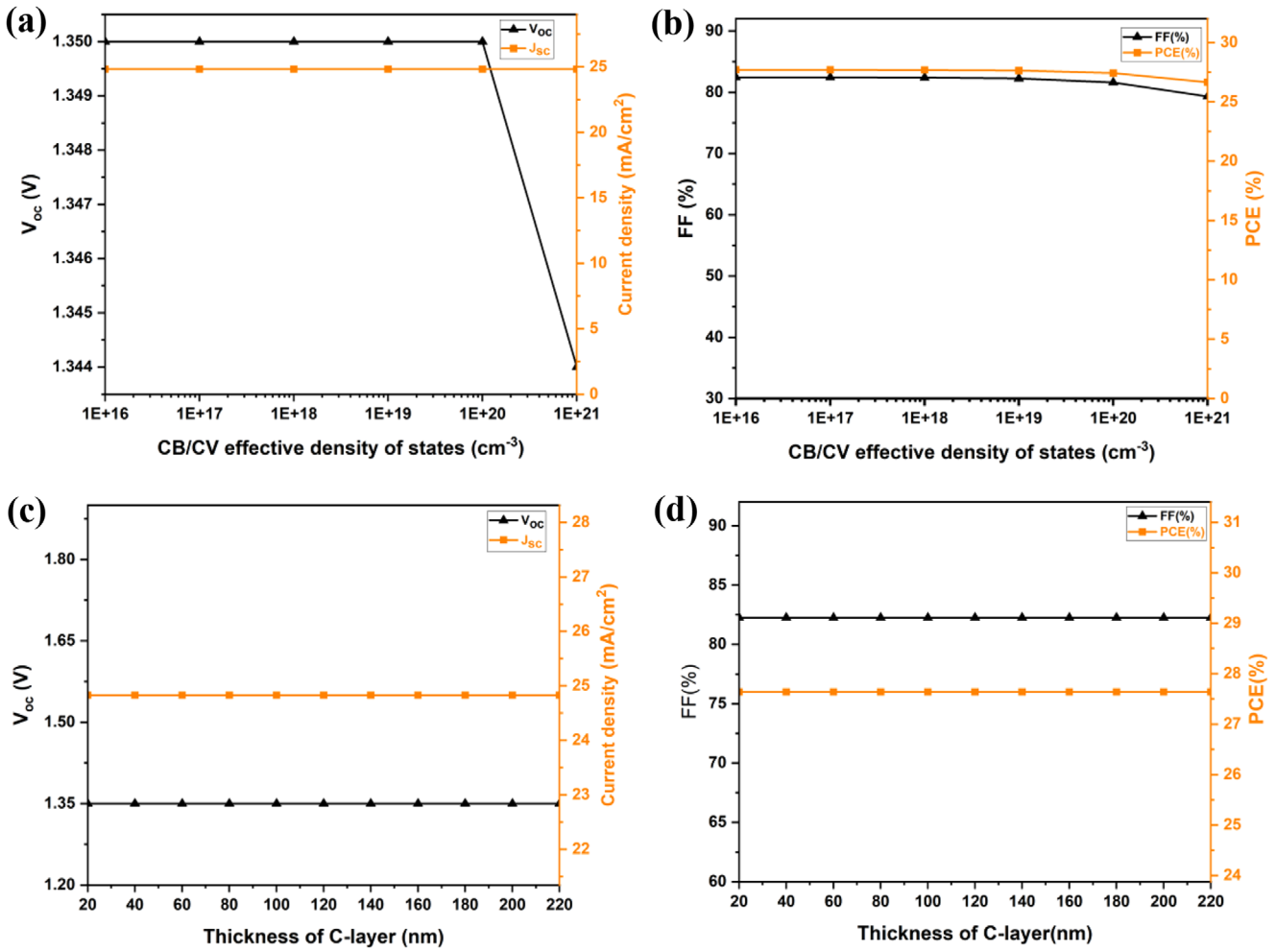

Figure 3. Impact of the density of states a,b) and the thickness c,d) of the carbon interlayer on the PSC parameters: J_{sc}, V_{oc} FF, and PCE. For (a,b), a carbon interlayer of 70 nm was used.

The simulations in the next sections will keep these parameters constant.

2.4. Impact of the Properties of the Carbon Nanostructure Used as Interlayer

To rationalize the role of the characteristics of carbon nanostructures as interlayers to the HTL in PSCs through numerical simulations with SCAPS-1D, we have screened two parameters; namely the electronic density of states and the optical characteristics of the carbon materials. The effective density of states (DOS) of the conduction and valence bands in a given material is crucial in determining the balance between radiative and nonradiative recombination processes. For carbon nanostructures, the electronic density of states in the conduction and valence bands varies significantly depending on the dominant hybridization of the carbon atoms and the presence of structural defects or dopants. To account for the variability of the density of states upon the nature of the carbon materials, we have screened this parameter in the range 10^{16}–10^{21}cm^{-3}eV^{-1}, which corresponds to values reported for carbons with different dominant hybridization states. For example, DOS values for the valence band ranging between 10^{16} and 10^{18} cm^{-3}eV^{-1} have been reported for amorphous and hydrogenated carbons; 10^{21}cm^{-3}eV^{-1} for carbon blacks; 10^{21}–10^{22} cm^{-3}eV^{-1} for porous carbons doped with heteroatoms, and between 10^{17} and 10^{20} cm^{-3}eV^{-1} for graphenes and carbon nanotubes.[36–39]

The impact on V_{oc}, J_{sc}, FF, and PCE is illustrated in **Figure 3**a,b. Our simulations show that the DOS of the carbon interlayer does not seem to have a strong impact on the open circuit potential and the current density of the device, with almost constant values for both parameters with the DOS varied from 10^{16} to 10^{20} cm^{-3} eV (Figure 4a). Only above 10^{20} cm^{-3} a slightly lower V_{oc} was observed, although the decrease accounted for ca. 0.7%. This suggests a good alignment of the energy levels at this interface. Similarly, minor modifications were obtained for the FF (Figure 3b) with a 4% fall that may be attributed to a low shunt resistance and high series resistance in the device. On the other hand, the PCE decreased by 3.8% as the DOS increased. Considering the evolution of the four parameters, optimum values of DOS for carbon interlayers to the HTL would be in the range 10^{17}–10^{20} cm^{-3} eV^{-1}.

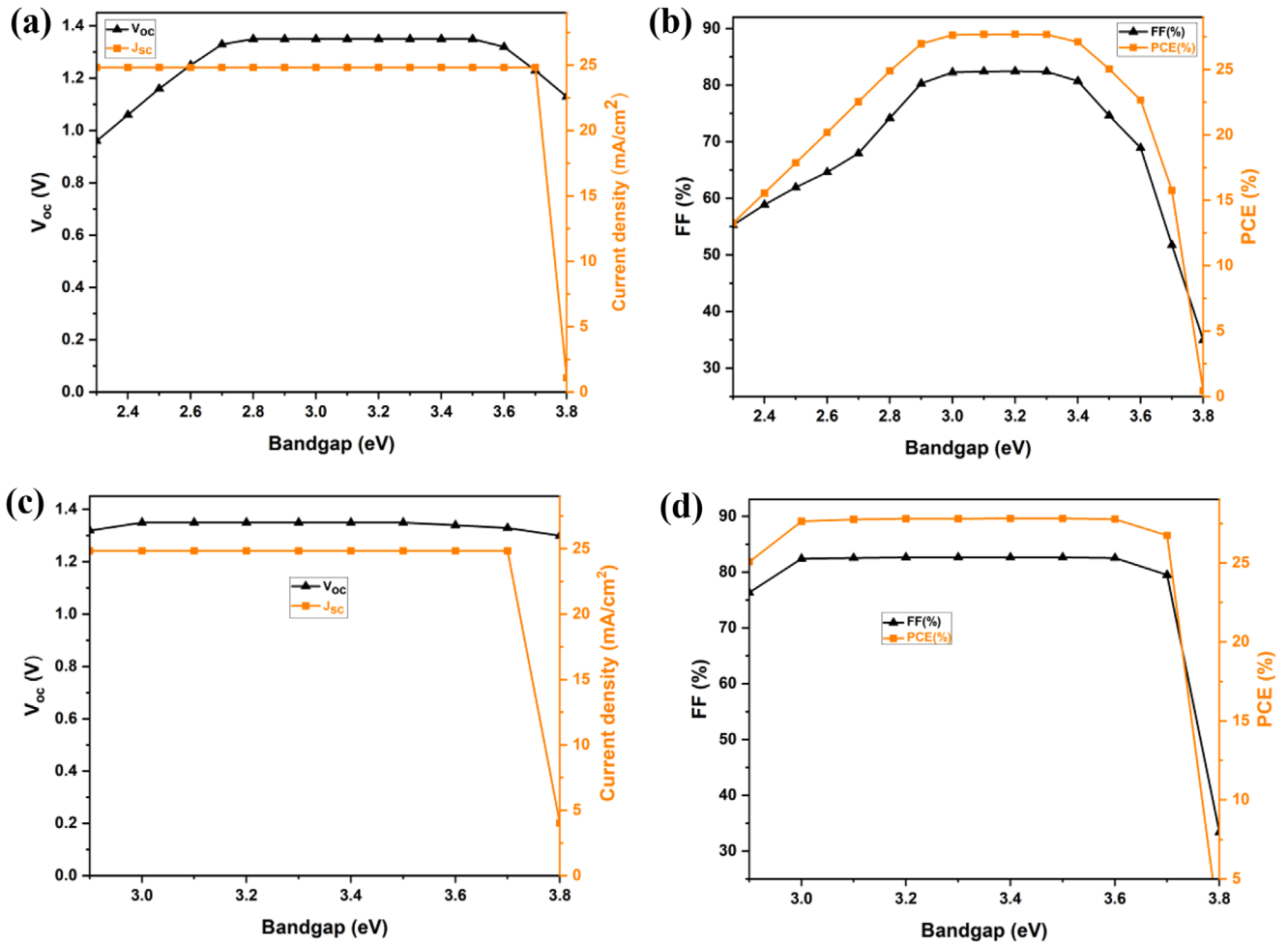

Figure 4. Effect of the bandgap of the carbon nanostructure used as interlayer on key performance indicators of the solar cell device: a,c) J_{sc} and V_{oc} b,d) FF and PCE for different configurations: (a,b) AL/HTL-carbon interlayer/BCM; (c,d) AL/carbon interlayer-HTL/BCM.

For further investigations in the next sections, the effective density of states of the conduction band (CB) and the valence band (VB) will be set to 10^{18} cm^{-3}.

Figure 3c,d show the impact of the thickness of the carbon interlayer incorporated into the HTL on the performance of the device. In this context, it is important to highlight that the overall thickness of the HTL can enhance the collection efficiency of the charge carriers and the efficiency of the light absorption, but it may also give rise to large contributions of series resistances.[40] For this reason, the thickness of the carbon interlayer was varied between 30 and 220 nm, while keeping constant the thickness of the Spiro-OMeTAD layer to 100 nm. Our simulations show that for the explored range, the thickness of the carbon layer does not seem to have any impact on the performance indicators of the device. This is in line with studies reporting rather constant performance parameters of the solar cells when the thickness of HTL (Spiro-OMeTAD) is varied between 100 and 600 nm.[40] Hence, an overall thickness of 150 nm for the hybrid HTL/C-interlayer was fixed, accounting for 50 nm of the carbon interlayer and 100 nm of the HTL.

Figure 4 shows the variation of the performance indicators of the solar cell with the band gap of the carbon interlayer. This parameter has been used to evaluate the most adequate carbon nanostructure as an interlayer to the HTL. In our numerical simulations, we have varied the bandgap of the carbon nanostructure from 2.3 to 3.8 eV for two configurations: interface HTL/C-interlayer/BCM (Figure 4a,b) and interface C-interlayer/HTL/BCM (Figure 4c,d). This bandgap range was chosen according to the experimental values reported in the literature for a diversity of carbon nanostructures (such as amorphous carbons, porous carbons, carbon blacks, carbon nanotubes, and graphene derivatives) with varied structure and composition.[41,42–44] With the exception of the highest bandgap value, the bandgap of the carbon interlayer does not seem to affect the short-circuit current density of the cell (that remained constant at 24.83 mA cm^{-2}) regardless of the configuration of the interface. In contrast, the current density drastically decreased to almost zero for the highest band gap value. This behavior suggests an energy level misalignment, where extraction of the holes becomes very unfavorable. For band gap values above 3.8 eV, the simulations in SCAPS did not converge, which we have interpreted as poor efficiency of the solar cells.

For the open circuit potential, the configuration of the interface is important. For the HTL/C-interlayer/BMC interface

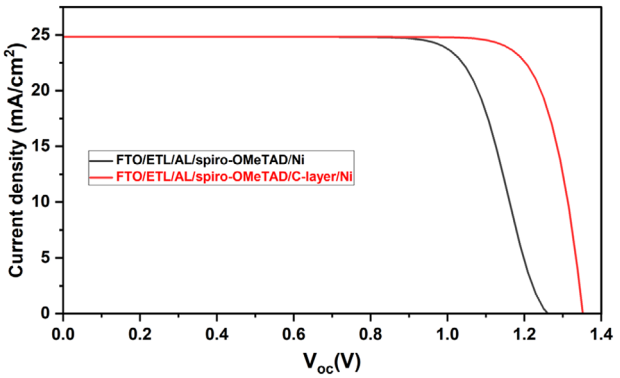

Figure 5. Simulated *I–V* curves of FTO/TiO_2/$MAPbI_3$/HTL/Ni with and without C-interlayer.

(Figure 4a), the V_{oc} reached a plateau of maximum values for bandgaps between 2.8 and 3.5 eV, showing a decreasing trend above and below those limits (i.e., holes cannot migrate easily to the BCM). In those optimal conditions, the V_{oc} for the HTL/C-interlayer/BCM configuration is 5.18% higher than that of HTL/BCM without carbon interlayer. The improvement in the V_{oc} confirms the better hole extraction of the HTL/C-interlayer interface, suggesting that the role of the carbon interlayer is to reduce the accumulation of holes in spiro-OMeTAD, by donating electronic density. For the interface C-interlayer/HTL/BCM (Figure 4c), the V_{oc} remained rather unchanged, with a value similar to that of the above-mentioned configuration HTL/C-interlayer/BCM. The location of the carbon interlayer is also important for the FF and PCE parameters. When the carbon interlayer is located between the HTL and the BCM, the FF and PCE are significantly modified (Figure 4b,d).

The FF increased (from 55.29 to 82.39%) as the bandgap rose up to 3.3 eV (accounting for a 1.5 fold increase), and the PCE increased from 13.27% up to 27.68%. Above 3.3 eV, the performance indicators of the device were very poor, both in terms of FF and PCE. The increase in the FF indicates a relatively lower contact resistance (R_c) in the device upon the incorporation of the carbon interlayer, and/or a significantly improved hole extraction. This is in agreement with the observed trends of V_{oc} and current density. It is interesting to note that bandgap values between 2.1 and 3.4 eV have been reported for amorphous carbon nanostructures with a high density of structural defects (such as porous carbons, and carbon blacks) and carbon nanotubes.[41–44] The best performance in carbon materials with optical bandgaps between 2.7 and 3.5 eV indicates the importance of the nature of the carbon nanostructure since the optical energy gap depends on the hybridization state of the carbon atoms (sp^2/sp^3 ratio).[41] According to the literature, high optical bandgaps correspond to carbon nanostructures with low sp^2/sp^3 ratios, pointing out the importance of structures with partially bounded graphitic regions combining π states in sp^2 clusters and defective sp^3 sites.[41,45–48] Wide optical bandgaps in the HTL favor the creation of an energy barrier for the electrons, acting as passivation of the perovskite, thus preventing back electron transfer. Similar observations have been reported for other carbon nanostructures.[49,21–23]

Figure 5 shows a comparison of the *I–V* curves of an FTO/TiO_2/$MAPbI_3$/HTL/Ni cell incorporating the carbon nanostructure as an interlayer to Spiro-OMeTAD as HTL or as HTL alone. The optimized parameters and output characteristics of the device for the different layers used in the numerical simulations are compiled in **Table 2**. As seen, when the spiro-OMeTAD material alone is used as HTL, the device displayed a V_{oc} (ca. 1.28 V) ≈1.5 times lower than that computed when the hybrid carbon interlayer-spiro-OMeTAD was used as HTL (ca. 1.35 V). It is also worth mentioning the higher PCE of the cell built with the carbon interlayer, compared to Spiro-OMeTAD alone as HTL.

While the current density of these configurations was similar, the FF increased, and the *I–V* curves of the device built using carbon nanostructures of varied characteristics as HTL alone (i.e., FTO/TiO_2/$MAPbI_3$/Carbon/Ni) are shown in the Supporting Information (Figures S1 and S2, and Table S1, Supporting Information). The simulations demonstrated a gradual increase in the Voc, FF, and PCE with the bandgap of the carbon interlayer, reaching a maximum performance for values ranging from 2.8 to 3.2 eV.

The improved Voc upon the incorporation of the carbon interlayer indicates a more efficient hole extraction. This can be explained as a reduction in the accumulation of the charge,[29] a better level alignment between the HTL/C-interlayer and the back contact metal, and/or a decreased resistance contact. The more efficient extraction of the holes is mostly likely attributed to the high electronic density of carbon materials due to the rich carbon atoms in the sp^2 configuration.[49,23]

Table 2. Performance parameters of an FTO/ETL/AL/HTL/BCM solar cell vary the nature of the metal used as back contact metal.

	C-interlayer		Absorber layer	
Absorber layer thickness [nm]	– – – – –		700	
Bandgap, E_g [eV]	3		1.5	
Carbon layer thickness(nm)	50		– – – – –	
CB effective density of states, N_c[cm^{-3}]	2.2×10^{18}		2.2×10^{18}	
VB effective density of states, N_v [cm^{-3}]	2.2×10^{18}		1.8×10^{21}	
Total defect density at ETL/perovskite, and perovskite/HTL interfaces, N_t[cm^{-3}]	$10^{10}/10^{10}$		$10^{10}/10^{10}$	
PSC key operating parameters	V_{oc}(V)	J_{sc}(mA/cm^2)	FF (%)	PCE (%)
FTO/TiO_2/$MAPbI_3$/spiro-OMeTAD/Ni	1.28	24.83	78.94	25.31
FTO/TiO_2/$MAPbI_3$/spiro-OMeTAD-Carbon interlayer/Ni	1.35	24.83	82.26	27.64
FTO/TiO_2/$MAPbI_3$/ Carbon interlayer-spiro-OMeTAD /Ni	1.34	24.83	82.42	27.63

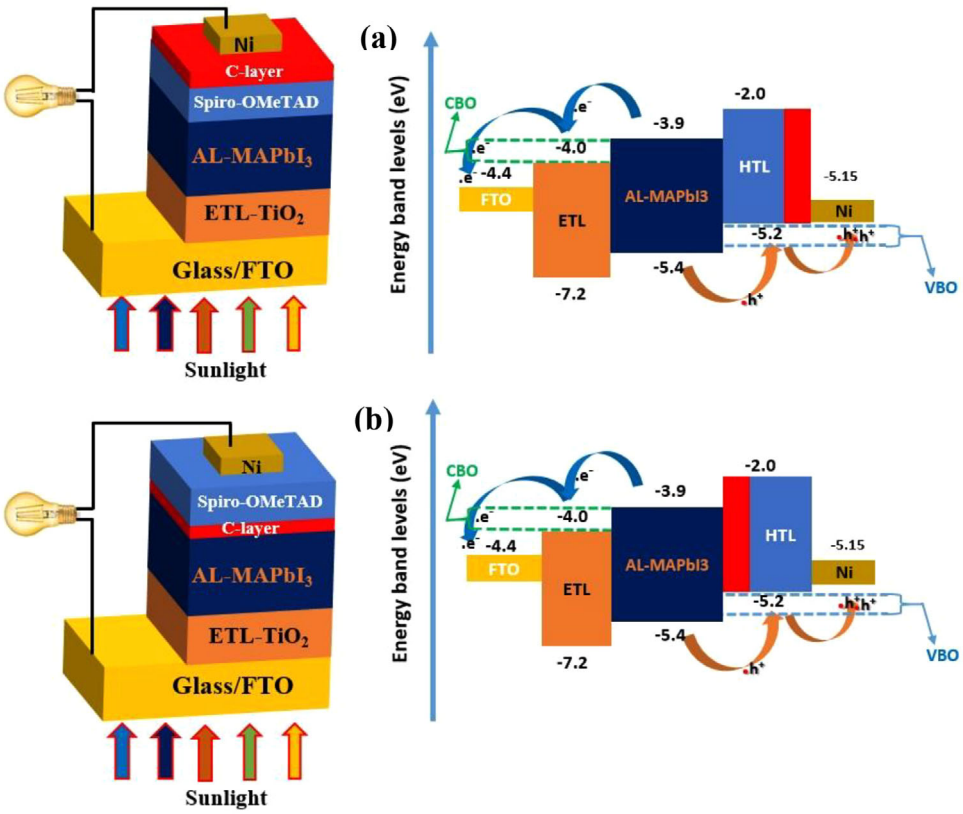

Figure 6. Schematic structure of the devices and energy band diagram of the studied perovskite devices: a) FTO/ETL/AL/HTL-carbon interlayer/Ni; b) FTO/ETL/AL/carbon interlayer-HTL/Ni.

Table 3. Parameters for back and front contacts used in SCAP-1D.

Parameter	Back Contact	Front contact
Surface recombination velocity of electrons [cm $^{-1}$s]	1.00E + 5	1.00E + 7
Surface recombination velocity of holes [cm $^{-1}$s]	1.00E + 7	1.00E + 5
Metal work function [eV]	5.15	4.4
Majority carrier barrier height relative to E_f [eV]	0.15	0.4
Minority carrier barrier height relative to E_v [eV]	0.093	0.45

Regarding the position, we attribute the better hole extraction when the carbon interlayer is located between the spiro-OMeTAD and the BCM to the fact that spiro-OMeTAD alone shows a better extraction capacity and better band alignment than the carbon material itself, as inferred by the results obtained when both (spiro-OMeTAD or the carbon material) were used as HTL alone. Thus, the role of the carbon interlayer is to reduce the accumulation of holes in spiro-OMeTAD, by donating the necessary electronic density (an intrinsic characteristic of most carbon materials is their rich electronic density). The electrical conductivity also plays an important role in the hole extraction efficiency of the HTL from the perovskite layer, and the C-interlayer has a higher conductivity than spiro-OMeTAD. Moreover, the carbon interlayer also provides a lower resistance at the HTL/back contact interface, which benefits the overall cell indicators by decreasing the overall series resistance of the cell.

3. Conclusion

This work has evaluated the use of carbon nanostructures of varied nature as interlayers of the hole transport layer in perovskite solar cells with a regular n-i-p stacked structure (FTO/TiO_2/$MAPbI_3$/Spiro-OMeTAD/Ni), using numerical simulations. The carbon interlayer was introduced in the HTL using two configurations: between the active layer and the spiro-OMeTAD HTL and between the latter and the back metal contact. Our simulations show that the defect density at the ETL/perovskite and the perovskite/HTL interfaces is important to reach high V_{oc} and FF, demonstrating the importance of the choice of the material to be used as interlayer to those interfaces. The thickness of the carbon interlayer does not affect the performance of the solar cell, but it is important to consider the bandgap of the carbon nanostructure to reach an adequate band alignment with the HTL. Our simulations demonstrate that carbon nanostructures with optical bandgap in the range of 2.7–3.5 eV significantly enhanced the open-circuit voltage and fill factor of the devices. As a result, an overall enhancement of the power conversion efficiency by more than 2.3% is achieved. These values of bandgap correspond to amorphous carbons, nanoporous carbons, and carbon nanotubes. Other carbon nanostructures resulted in lower hole extraction efficiencies. The configuration of the interface is also important, with a favorable valence band offset at the HTL/C-interlayer/BCM interface, which results in an increase of 5.18% in the open circuit voltage

Table 4. Selected properties of the materials used in the different layers of the perovskite solar cell were investigated, and used as input in the simulations.

Parameter [unit]	FTO	ETL (TiO_2)	AL [$MAPbI_3$]	HTL [Spiro-OMeTAD]	Carbon Interlayer
Thickness (*nm*)	500	100	300 – 700	100	50–220nm
Bandgap, $E_g(eV)$	3.5	3.2	1.5	3.2	2.1 – 3.7
Electron affinity *E*, χ (*eV*)	4.4	4	3.9	2	2.3
Dielectric permittivity (ε_r)	9	9	6.5	3	10
CB effective density of states N_c [cm^{-3}]	2.0×10^{18}	2.2×10^{18}	2.2×10^{18}	2.2×10^{18}	2.2×10^{16} – 2.2×10^{21}
VB effective density of states N_v [cm^{-3}]	1.0×10^{19}	1.8×10^{19}	1.8×10^{19}	1.8×10^{19}	1.8×10^{16} – 2.2×10^{21}
Electron thermal velocity [$cm.s^{-1}$]	1.0×10^{7}	1.0×10^{7}	1.0×10^{7}	1.0×10^{7}	5.2×10^{7}
Hole thermal velocity [$cm.s^{-1}$]	1.0×10^{7}	1.0×10^{7}	1.0×10^{7}	1.0×10^{7}	5.0×10^{7}
Electron mobility, μ_n[$.V^{-1}.s^{-1}$]	20	20	20	1.0×10^{-4}	26
Hole mobility, μ_p[$cm^2.V^{-1}.s^{-1}$]	10	10	2	1.0×10^{-4}	123
Shallow donor density, N_D[cm^{-3}]	2.0×10^{19}	1.0×10^{18}	1.0×10^{13}	———	———
Shallow acceptor density, N_A[cm^{-3}]	———	———	———	2.0×10^{19}	2.0×10^{18}
Total defect density, N_t[cm^{-3}]	1.0×10^{15}	1.0×10^{15}	2.5×10^{13}	2.5×10^{15}	2.5×10^{15}

Table 5. Defect parameters of the ETL/perovskite and perovskite/HTL interfaces investigated.

	Defect type	Capture cross: section electrons/holes [cm^2]	Energetic distribution	Reference for defect energy level, E_t	Energy with respect to a reference (eV)	Total density energies (cm^{-2})	Total defect density (cm^{-2})
ETL/ AL	Neutral	1.0×10^{-19}	Single	Above the highest E_v	0.600	1.0×10^{10}	10^{10} (variable)
HTL/ AL	Neutral	1.0×10^{-19}	Single	Above the highest E_v	0.600	1.0×10^{10}	10^{10} (variable)

of the device. Our ongoing studies are directed to validate experimentally the outcome of these numerical simulations by incorporating the carbon interlayer in the optimized position pointed out in this work, while varying the nature of the carbon nanostructures. Further studies should also be directed to consider other aspects such as minimizing trap-assisted recombination reducing series and increasing shunt resistances of the perovskite devices, if the theoretical limit of these materials is to be reached.

4. Experimental Section

Numerical Modeling Using SCAPS-1D: In this study, version 3.3.09 of Solar Cell Capacitance Simulator-1Dimension (SCAPS-1D) was used. SCAPS is a 1D software tool capable of designing solar cells up to seven layers, developed by Ghent University in Belgium.[50,51] It is based on the resolution of Poisson's and continuity equations to obtain current–voltage characteristics. By applying appropriate boundary conditions at interfaces and contacts, the program solves the coupled Poisson's differential Equation 1 which links charges to electrostatic potential. Additionally, it addresses continuity differential equations for free electrons and holes in the conduction and valence bands given by Equations 2 and 3.

$$\frac{d}{dx}\left(\varepsilon\varepsilon_0\frac{d\psi(x)}{dx}\right) = -q\left(p(x) - n(x) + N_D^+ - N_A^- + \rho_p - \rho_n\right) \quad (1)$$

$$\left(\frac{1}{q}\right)\frac{\partial J_n}{\partial x} - U_n + G = \frac{\partial n}{\partial t} \quad (2)$$

$$-\left(\frac{1}{q}\right)\frac{\partial J_p}{\partial x} - U_p + G = \frac{\partial p}{\partial t} \quad (3)$$

where, ψ is the electric potential, ε *and* ε_0 the relative and vacuum permittivities, n and p, the densities of free charge carriers, N_D^+, N_A^- represent the densities of ionized donors and acceptors, ρ_p, ρ_n are hole and electron trap concentrations respectively, q is the elementary charge, U_n/U_p, and G are respectively recombination and generation rates. The density of diffusion and drift currents produced by electrons and holes can be expressed by Equation 4.

$$J_{n,p} = nq\mu_n E_{Fn} + qD_n\frac{\partial n}{\partial x} + pq\mu_p E_{Fp} + qD_p\frac{\partial p}{\partial x} \quad (4)$$

where, $J_{n,p}$ is the photocurrent of electron and hole carriers across a section, μ_n *and* μ_p are respectively electrons and holes mobilities, and E_{Fn}, E_{Fp} are the energies of the Fermi levels.

The numerical modeling with SCAPS-1D includes all the different steps involved in a solar cell operation (namely photon absorption, exciton generation, and separation, charge transfer, and recombination) by adequate equations. The photon-induced charge carrier generation rate is expressed by Equation 5.[52]

$$G(\lambda, x) = \int \alpha(\lambda)\times\phi(\lambda)\times e^{-(\alpha(\lambda)x)}d\lambda \quad (5)$$

where λ is the wavelength, α the absorption coefficient of the absorber layer, and x its thickness. In our simulations, α for the perovskite absorber was set as a constant ($10^5 cm^{-1}$).[53]

The trap-assisted Shockley–Read–Hall (SRH) recombination and charge recombination rate (due to non-ideal properties (defects) in perovskites) were evaluated by Equations 6 and 7.[54,52]

$$R^{SRH} = \frac{np - n_i^2}{\tau_n(p + p_t) + \tau_p(n + n_t)} \quad (6)$$

$$R = r\times\left(n\times p - n_i^2\right) \quad (7)$$

where, n_t, p_t are equilibrium electron and hole concentration, respectively given by: $n_t = N_c\exp[-(E_C - E_d)/(kT)]$ and

$p_t = N_V \exp[-(E_V - E_d)/(kT)]$, R is the recombination rate, r is a recombination constant and n_i the intrinsic density.

Following iterative solving of those equations, the main photovoltaic parameters of the solar cell, such as open-circuit voltage (V_{OC}), fill factor (FF), current density (J_{SC}), and power conversion efficiency (PCE) are calculated by the following Equations.

$$V_{oc} = \frac{nkT}{q} ln\left(\frac{J_{sc}}{J_0} + 1\right) \tag{8}$$

with J_{sc}, the light-generated current and J_0 the saturation current density is given by Equation 6.

$$J_0 = qN_vN_c\left(\frac{1}{N_A}\left(\frac{D_n}{\tau_n}\right)^{\frac{1}{2}} + \frac{1}{N_D}\left(\frac{D_p}{\tau_p}\right)^{\frac{1}{2}}\right)e^{-\frac{E_g}{k_BT}} \tag{9}$$

where, N_c, N_v are the effective density of states of electrons and holes, respectively; D_n and D_p the diffusion coefficients, k_B is Boltzmann constant, and T the temperature. The fill factor (FF) is the ratio between the maximum values $V_{max} \times J_{max}$ and the theoretical power $V_{OC} \times J_{SC}$ as shown in Equation 7:

$$FF = \frac{V_{max} \times J_{max}}{V_{oc} \times J_{sc}} \tag{10}$$

Finally, the PCE of the solar device is calculated as follows:

$$\eta = \frac{V_{OC} \times J_{SC} \times FF}{P_{inc}} \tag{11}$$

Numerical Modeling Parameters: A perovskite solar cell with a regular n-i-p stacked configuration is selected (FTO/ ETL/AL/HTL/BCM), where the active layer is $MAPbI_3$ (i.e., methylammonium lead iodide, one of the first perovskite materials used in perovskite solar cells, still widely explored), the ETL is TiO_2, the HTL is spiro-OMeTAD or spiro-OMeTAD modified with the carbon interlayer. The BCM has been optimized. Figure 6a,b show the stacking device structure and the energy band alignment of the different materials of the solar cell device, respectively. All the simulations were performed under standard test conditions (STC):, i.e., for an air mass coefficient of 1.5(AM1.5), an incident power of 100 mW cm^{-2}, and at 300 K. The FTO/ETL and HTL/BCM interfaces were considered as ohmic contacts. The effect of series and shunt resistances was also introduced in the device simulation, setting the values at, respectively, 0.5 and 10^4 $\Omega\, cm^{-2}$. The parameters tested for back and front contact are listed in Table 3.

The parameters used to simulate the materials of the different layers composing the PSCs are compiled in **Table 4**. Several groups have reported similar values in the literature.[25,55–57,24,30] **Table 5** shows properties of the ETL/$MAPbI_3$ and $MAPbI_3$/HTL interfaces.

Supporting Information

Supporting Information is available from the Wiley Online Library or from the author.

Acknowledgements

The authors thank the financial support of the LEAP-RE program (grant NANOSOLARCELLS). W.F. thanks the Bank Republic of Haïti (BRH) and the French embassy of Haïti for his PhD fellowship.

Conflict of Interest

The authors declare no conflict of interest.

Data Availability Statement

The data that support the findings of this study are available from the corresponding author upon reasonable request.

Keywords

additives engineering, carbon materials, hole transport layers, hybrid HTLs, interface design, low-cost solar cells, perovskite solar cells

Received: July 31, 2024
Revised: September 2, 2024
Published online:

[1] A. Raj, M. Kumar, A. Anshul, *Mater. Today Chem.* **2021**, *22*, 100595.
[2] J. Reilly, *Rev. D'économie Dév* **2015**, *23*, 19.
[3] J. Zarocostas, *Lancet* **2022**, *400*, 148.
[4] M. Thirugnanasambandam, S. Iniyan, R. Goic, *Renew. Sustain. Energy Rev.* **2010**, *14*, 312.
[5] G. Giorgi, K. Yamashita, *J. Mater. Chem. A* **2015**, *3*, 8981.
[6] A. Kojima, K. Teshima, Y. Shirai, T. Miyasaka, *J. Am. Chem. Soc.* **2009**, *131*, 6050.
[7] R. K. Koech, R. Ichwani, D. Oyewole, M. Kigozi, D. Amune, D. M. Sanni, S. Adeniji, K. Oyewole, A. Bello, E. Ntsoenzok, *Energies* **2021**, *14*, 7870.
[8] "Interactive Best Research-Cell Efficiency Chart," can be found under https://www.nrel.gov/pv/interactive-cell-efficiency.html.
[9] Y. Zheng, Y. Li, R. Zhuang, X. Wu, C. Tian, A. Sun, C. Chen, Y. Guo, Y. Hua, K. Meng, *Energy Environ. Sci.* **2024**, *17*, 1153.
[10] E. M. Hutter, M. C. Gélvez-Rueda, A. Osherov, V. Bulović, F. C. Grozema, S. D. Stranks, T. J. Savenije, *Nat. Mater.* **2017**, *16*, 115.
[11] S. A. Kulkarni, T. Baikie, P. P. Boix, N. Yantara, N. Mathews, S. Mhaisalkar, *J. Mater. Chem. A* **2014**, *2*, 9221.
[12] M. Hatamvand, P. Vivo, M. Liu, M. Tayyab, D. Dastan, X. Cai, M. Chen, Y. Zhan, Y. Chen, W. Huang, *Vacuum* **2023**, *214*, 112076.
[13] G. Grancini, C. Roldán-Carmona, I. Zimmermann, E. Mosconi, X. Lee, D. Martineau, S. Narbey, F. Oswald, F. De Angelis, M. Graetzel, *Nat. Commun.* **2017**, *8*, 15684.
[14] E. Widianto, E. S. Rosa, K. Triyana, N. M. Nursam, I. Santoso, *Adv. Nat. Sci. Nanosci. Nanotechnol.* **2021**, *12*, 035001.
[15] P. Mariani, L. Najafi, G. Bianca, M. I. Zappia, L. Gabatel, A. Agresti, S. Pescetelli, A. Di Carlo, S. Bellani, F. Bonaccorso, *ACS Appl. Mater. Interfaces* **2021**, *13*, 22368.
[16] N. Ahn, I. Jeon, J. Yoon, E. I. Kauppinen, Y. Matsuo, S. Maruyama, M. Choi, *J. Mater. Chem. A* **2018**, *6*, 1382.
[17] C. Tian, A. Mei, S. Zhang, H. Tian, S. Liu, F. Qin, Y. Xiong, Y. Rong, Y. Hu, Y. Zhou, *Nano Energy* **2018**, *53*, 160.
[18] A. K. Kang, M. H. Zandi, N. E. Gorji, *Opt. Quantum Electron.* **2019**, *51*, 91.
[19] E. C. Kohlrausch, D. de Vasconcelos Freitas, da C. I. Silva Filho, L. Fernandes Loguercio, L. A. Santa-Cruz, L. J. Lins Maciel, M. Z. Oliveira, C. I. do L dos Santos, G. Machado, *Energy Technol.* **2023**, *11*, 2200676.
[20] E. Muchuweni, B. S. Martincigh, V. O. Nyamori, *Adv. Energy Sustain. Res.* **2021**, *2*, 2100050.
[21] R. Chen, Y. Feng, C. Zhang, M. Wang, L. Jing, C. Ma, J. Bian, Y. Shi, *J. Mater. Chem. C* **2020**, *8*, 9262.
[22] A. Saeed, M. M. Salah, A. Zekry, M. Mousa, A. Shaker, M. Abouelatta, F. Z. Amer, R. I. Mubarak, D. S. Louis, *Energies* **2023**, *16*, 1676.
[23] E. Jokar, Z. Y. Huang, S. Narra, C. Wang, V. Kattoor, C. Chung, E. W. Diau, *Adv. Energy Mater.* **2018**, *8*, 1701640.

[24] S. Sakib, M. Y. M. Noor, M. R. Salim, A. S. Abdullah, A. I. Azmi, M. H. Ibrahim, M. H. Ibrahim, *Mater. Today Proc* **2023**, *80*, 1022.
[25] J. W. Xiao, C. Shi, C. Zhou, D. Zhang, Y. Li, Q. Chen, *Sol. RRL* **2017**, *1*, 1700082.
[26] H. B. Michaelson, *J. Appl. Phys.* **1977**, *48*, 4729.
[27] K. Domanski, J. P. Correa-Baena, N. Mine, M. K. Nazeeruddin, A. Abate, M. Saliba, W. Tress, A. Hagfeldt, M. Grätzel, *ACS Nano* **2016**, *10*, 6306.
[28] D. Jayan K, V. Sebastian, *Adv. Theory Simul.* **2021**, *4*, 2100027.
[29] N. Zhang, C. Wang, T. Li, Y. Li, X. Yu, L. Liang, H. Bao, P. Gao, *Chem. Inorg. Mater.* **2024**, *2*, 100031.
[30] E. Widianto, E. S. Rosa, K. Triyana, N. M. Nursam, I. Santoso, *Opt. Mater.* **2021**, *121*, 111584.
[31] J. Wu, J. Shi, Y. Li, H. Li, H. Wu, Y. Luo, D. Li, Q. Meng, *Adv. Energy Mater.* **2019**, *9*, 1901352.
[32] G. Meng, N. K. Elumalai, H. Mehdizadeh-Rad, K. S. Ram, D. D. Y. Setsoafia, D. Ompong, *Adv. Theory Simul.* **2024**, *7*, 2300784.
[33] A. S. Chouhan, N. P. Jasti, S. Avasthi, *Mater. Lett.* **2018**, *221*, 150.
[34] M. S. S. Basyoni, M. M. Salah, M. Mousa, A. Shaker, A. Zekry, M. Abouelatta, M. T. Alshammari, K. A. Al-Dhlan, C. Gontrand, *IEEE Access* **2021**, *9*, 130221.
[35] X. Wang, J. Wu, Y. Yang, G. Li, Z. Song, X. Liu, W. Sun, Z. Lan, P. Gao, *J. Energy Chem.* **2021**, *61*, 386.
[36] V. S. Veerasamy, G. A. J. Amaratunga, C. A. Davis, W. I. Milne, P. Hewitt, M. Weiler, *Solid-State Electron.* **1994**, *37*, 319.
[37] B. Bera, A. Chakraborty, T. Kar, P. Leuaa, M. Neergat, *J. Phys. Chem. C* **2017**, *121*, 20850.
[38] S. Dröscher, P. Roulleau, F. Molitor, P. Studerus, C. Stampfer, K. Ensslin, T. Ihn, *Phys. Scr.* **2012**, *2012*, 014009.
[39] J. D. Wiggins-Camacho, K. J. Stevenson, *J. Phys. Chem. C* **2009**, *113*, 19082.
[40] N. Marinova, W. Tress, R. Humphry-Baker, M. I. Dar, V. Bojinov, S. M. Zakeeruddin, M. K. Nazeeruddin, M. Grätzel, *ACS Nano* **2015**, *9*, 4200.
[41] T. J. Bandosz, C. O. Ania, *Adv. Sci.* **2018**, *5*, 1800293.
[42] G. D. Gesesse, A. Gomis-Berenguer, M. F. Barthe, C. O. Ania, *J. Photochem. Photobiol. Chem.* **2020**, *398*, 112622.
[43] I. Velo-Gala, J. J. López-Peñalver, M. Sánchez-Polo, J. Rivera-Utrilla, *Appl. Catal. B Environ.* **2013**, *142*, 694.
[44] Y. Song, H. Hu, M. Feng, H. Zhan, *ACS Appl. Mater. Interfaces* **2015**, *7*, 25793.
[45] J. Robertson, E. P. O'Reilly, *Phys. Rev. B* **1987**, *35*, 2946.
[46] J. Robertson, *Phys. Rev. Lett.* **1992**, *68*, 220.
[47] A. D. Modestov, J. Gun, O. Lev, *Surf. Sci.* **1998**, *417*, 311.
[48] Y. Miyajima, Y. Tison, C. E. Giusca, V. Stolojan, H. Watanabe, H. Habuchi, S. J. Henley, J. M. Shannon, S. R. P. Silva, *Carbon* **2011**, *49*, 5229.
[49] Z. Li, S. A. Kulkarni, P. P. Boix, E. Shi, A. Cao, K. Fu, S. K. Batabyal, J. Zhang, Q. Xiong, L. H. Wong, N. Mathews, S. G. Mhaisalkar, *ACS Nano* **2014**, *8*, 6797.
[50] M. Burgelman, P. Nollet, S. Degrave, *Thin Solid Films* **2000**, *361*, 527.
[51] M. Burgelman, K. Decock, S. Khelifi, A. Abass, *Thin Solid Films* **2013**, *535*, 296.
[52] Y. Zhou, A. Gray-Weale, *Phys. Chem. Chem. Phys.* **2016**, *18*, 4476.
[53] G. Xing, N. Mathews, S. Sun, S. S. Lim, Y. M. Lam, M. Grätzel, S. Mhaisalkar, T. C. Sum, *Science* **2013**, *342*, 344.
[54] A. K. Al-Mousoi, M. K. Mohammed, A. Kumar, R. Pandey, J. Madan, D. Dastan, M. K. Hossain, P. Sakthivel, Z. M. Yaseen, *Phys. Chem. Chem. Phys.* **2023**, *25*, 16459.
[55] G. M. Dzifack Kenfack, F. Tchangnwa Nya, A. Laref, *Int. J. Energy Res.* **2022**, *46*, 8962.
[56] H. Shen, D. A. Jacobs, Y. Wu, T. Duong, J. Peng, X. Wen, X. Fu, S. K. Karuturi, T. P. White, K. Weber, K. R. Catchpole, *J. Phys. Chem. Lett.* **2017**, *8*, 2672.
[57] T. Minemoto, Y. Kawano, T. Nishimura, J. Chantana, *Opt. Mater.* **2019**, *92*, 60.